Search for nucleon decay into charged antilepton plus meson in 0.316 megaton · years exposure of the Super-Kamiokande water Cherenkov detector

K. Abe,[1,38] C. Bronner,[1] G. Pronost,[1] Y. Hayato,[1,38] M. Ikeda,[1] K. Iyogi,[1] J. Kameda,[1,38] Y. Kato,[1] Y. Kishimoto,[1,38] Ll. Marti,[1] M. Miura,[1,38] S. Moriyama,[1,38] M. Nakahata,[1,38] Y. Nakano,[1] S. Nakayama,[1,38] Y. Okajima,[1] A. Orii,[1] H. Sekiya,[1,38] M. Shiozawa,[1,38] Y. Sonoda,[1] A. Takeda,[1,38] A. Takenaka,[1] H. Tanaka,[1] S. Tasaka,[1] T. Tomura,[1,38] R. Akutsu,[2] T. Kajita,[2,38] K. Kaneyuki,[2,38,*] Y. Nishimura,[2] K. Okumura,[2,38] K. M. Tsui,[2] L. Labarga,[3] P. Fernandez,[3] F. d. M. Blaszczyk,[4] J. Gustafson,[4] C. Kachulis,[4] E. Kearns,[4,38] J. L. Raaf,[4] J. L. Stone,[4,38] L. R. Sulak,[4] S. Berkman,[5] S. Tobayama,[5] M. Goldhaber,[6,*] M. Elnimr,[7] W. R. Kropp,[7] S. Mine,[7] S. Locke,[7] P. Weatherly,[7] M. B. Smy,[7,38] H. W. Sobel,[7,38] V. Takhistov,[7,†] K. S. Ganezer,[8] J. Hill,[8] J. Y. Kim,[9] I. T. Lim,[9] R. G. Park,[9] A. Himmel,[10] Z. Li,[10] E. O'Sullivan,[10] K. Scholberg,[10,38] C. W. Walter,[10,38] T. Ishizuka,[11] T. Nakamura,[12] J. S. Jang,[13] K. Choi,[14] J. G. Learned,[14] S. Matsuno,[14] S. N. Smith,[14] J. Amey,[15] R. P. Litchfield,[15] W. Y. Ma,[15] Y. Uchida,[15] M. O. Wascko,[15] S. Cao,[16] M. Friend,[16] T. Hasegawa,[16] T. Ishida,[16] T. Ishii,[16] T. Kobayashi,[16] T. Nakadaira,[16] K. Nakamura,[16,38] Y. Oyama,[16] K. Sakashita,[16] T. Sekiguchi,[16] T. Tsukamoto,[16] KE. Abe,[17] M. Hasegawa,[17] A. T. Suzuki,[17] Y. Takeuchi,[17,38] T. Yano,[17] T. Hayashino,[18] T. Hiraki,[18] S. Hirota,[18] K. Huang,[18] M. Jiang,[18] KE. Nakamura,[18] T. Nakaya,[18,38] B. Quilain,[18] N. D. Patel,[18] R. A. Wendell,[18,38] L. H. V. Anthony,[19] N. McCauley,[19] A. Pritchard,[19] Y. Fukuda,[20] Y. Itow,[21,22] M. Murase,[21] F. Muto,[21] P. Mijakowski,[23] K. Frankiewicz,[23] C. K. Jung,[24] X. Li,[24] J. L. Palomino,[24] G. Santucci,[24] C. Vilela,[24] M. J. Wilking,[24] C. Yanagisawa,[24,‡] S. Ito,[25] D. Fukuda,[25] H. Ishino,[25] A. Kibayashi,[25] Y. Koshio,[25,38] H. Nagata,[25] M. Sakuda,[25] C. Xu,[25] Y. Kuno,[26] D. Wark,[27,33] F. Di Lodovico,[28] B. Richards,[28] R. Tacik,[29,40] S. B. Kim,[30] A. Cole,[31] L. Thompson,[31] H. Okazawa,[32] Y. Choi,[34] K. Ito,[35] K. Nishijima,[35] M. Koshiba,[36] Y. Totsuka,[36,*] Y. Suda,[37] M. Yokoyama,[37,38] R. G. Calland,[38] M. Hartz,[38] K. Martens,[38] C. Shimpson,[38,27] Y. Suzuki,[38] M. R. Vagins,[38,7] J. F. Martin,[39] C. M. Nantais,[39] H. A. Tanaka,[39] A. Konaka,[40] S. Chen,[41] L. Wan,[41] Y. Zhang,[41] A. Minamino,[42] and R. J. Wilkes[43]

(The Super-Kamiokande Collaboration)

[1]*Kamioka Observatory, Institute for Cosmic Ray Research, University of Tokyo, Kamioka, Gifu 506-1205, Japan*
[2]*Research Center for Cosmic Neutrinos, Institute for Cosmic Ray Research, University of Tokyo, Kashiwa, Chiba 277-8582, Japan*
[3]*Department of Theoretical Physics, University Autonoma Madrid, 28049 Madrid, Spain*
[4]*Department of Physics, Boston University, Boston, MA 02215, USA*
[5]*Department of Physics and Astronomy, University of British Columbia, Vancouver, BC, V6T1Z4, Canada*
[6]*Physics Department, Brookhaven National Laboratory, Upton, NY 11973, USA*
[7]*Department of Physics and Astronomy, University of California, Irvine, Irvine, CA 92697-4575, USA*
[8]*Department of Physics, California State University, Dominguez Hills, Carson, CA 90747, USA*
[9]*Department of Physics, Chonnam National University, Kwangju 500-757, Korea*
[10]*Department of Physics, Duke University, Durham NC 27708, USA*
[11]*Junior College, Fukuoka Institute of Technology, Fukuoka, Fukuoka 811-0295, Japan*
[12]*Department of Physics, Gifu University, Gifu, Gifu 501-1193, Japan*
[13]*GIST College, Gwangju Institute of Science and Technology, Gwangju 500-712, Korea*
[14]*Department of Physics and Astronomy, University of Hawaii, Honolulu, HI 96822, USA*
[15]*Department of Physics, Imperial College London, London, SW7 2AZ, United Kingdom*
[16]*High Energy Accelerator Research Organization (KEK), Tsukuba, Ibaraki 305-0801, Japan*
[17]*Department of Physics, Kobe University, Kobe, Hyogo 657-8501, Japan*
[18]*Department of Physics, Kyoto University, Kyoto, Kyoto 606-8502, Japan*
[19]*Department of Physics, University of Liverpool, Liverpool, L69 7ZE, United Kingdom*
[20]*Department of Physics, Miyagi University of Education, Sendai, Miyagi 980-0845, Japan*
[21]*Institute for Space-Earth Enviromental Research, Nagoya University, Nagoya, Aichi 464-8602, Japan*
[22]*Kobayashi-Maskawa Institute for the Origin of Particles and the Universe, Nagoya University, Nagoya, Aichi 464-8602, Japan*
[23]*National Centre For Nuclear Research, 00-681 Warsaw, Poland*
[24]*Department of Physics and Astronomy, State University of New York at Stony Brook, NY 11794-3800, USA*
[25]*Department of Physics, Okayama University, Okayama, Okayama 700-8530, Japan*
[26]*Department of Physics, Osaka University, Toyonaka, Osaka 560-0043, Japan*
[27]*Department of Physics, Oxford University, Oxford, OX1 3PU, United Kingdom*

[28]*School of Physics and Astronomy, Queen Mary University of London, London, E1 4NS, United Kingdom*
[29]*Department of Physics, University of Regina, 3737 Wascana Parkway, Regina, SK, S4SOA2, Canada*
[30]*Department of Physics, Seoul National University, Seoul 151-742, Korea*
[31]*Department of Physics and Astronomy, University of Sheffield, S10 2TN, Sheffield, United Kingdom*
[32]*Department of Informatics in Social Welfare, Shizuoka University of Welfare, Yaizu, Shizuoka, 425-8611, Japan*
[33]*STFC, Rutherford Appleton Laboratory, Harwell Oxford, and Daresbury Laboratory, Warrington, OX11 0QX, United Kingdom*
[34]*Department of Physics, Sungkyunkwan University, Suwon 440-746, Korea*
[35]*Department of Physics, Tokai University, Hiratsuka, Kanagawa 259-1292, Japan*
[36]*The University of Tokyo, Bunkyo, Tokyo 113-0033, Japan*
[37]*Department of Physics, University of Tokyo, Bunkyo, Tokyo 113-0033, Japan*
[38]*Kavli Institute for the Physics and Mathematics of the Universe (WPI), The University of Tokyo Institutes for Advanced Study, University of Tokyo, Kashiwa, Chiba 277-8583, Japan*
[39]*Department of Physics, University of Toronto, ON, M5S 1A7, Canada*
[40]*TRIUMF, 4004 Wesbrook Mall, Vancouver, BC, V6T2A3, Canada*
[41]*Department of Engineering Physics, Tsinghua University, Beijing, 100084, China*
[42]*Faculty of Engineering, Yokohama National University, Yokohama, 240-8501, Japan*
[43]*Department of Physics, University of Washington, Seattle, WA 98195-1560, USA*
(Received 23 May 2017; published 24 July 2017)

We have searched for proton decays into a charged antilepton (e^+, μ^+) plus a meson (η, ρ^0, ω) and for neutron decays into a charged antilepton (e^+, μ^+) plus a meson (π^-, ρ^-) using Super-Kamiokande I-IV data, corresponding to 0.316 megaton · years of exposure. This measurement updates the previous published result by using 2.26 times more data and improved analysis methods. No significant evidence for nucleon decay is observed and lower limits on the partial lifetime of the nucleon are obtained. The limits range from 3×10^{31} to 1×10^{34} years at 90% confidence level, depending on the decay mode.

DOI: 10.1103/PhysRevD.96.012003

I. INTRODUCTION

A. Grand unification theories

The standard model of particle physics, based on the $\mathrm{SU}(3)_c \times \mathrm{SU}(2)_L \times \mathrm{U}(1)_Y$ gauge symmetry, seems to be an incomplete description of nature's structure of matter and forces. The standard model fails to include massive neutrinos or provide a satisfying explanation for charge quantization or the convergence of gauge couplings at high energy scales. These issues are addressed in grand unified theories (GUTs), which embed the standard model in a single unifying gauge group such as SU(5) [1] or SO(10) [2]. While numerous specific realizations of GUTs exist (see [3] for review), as a universal feature they predict nucleon decay, and therefore, baryon number violation. The gauge coupling unification scale is around $10^{15\text{–}16}$ GeV, which is unreachable with accelerators but can be explored by virtual processes that induce nucleon decay with lifetimes of $10^{32\text{–}35}$ years. The lower end of this lifetime range may yield observable event rates in long exposures of a large water Cherenkov detector such as Super-Kamiokande (SK).

The two benchmark nucleon decay modes $p \to e^+\pi^0$ and $p \to \bar{\nu}K^+$ are favored channels [4] in nonsupersymmetric GUTs and TeV-scale supersymmetric GUTs, respectively. However, depending on the model, the branching ratios for nucleon decay channels vary and different decay modes can dominate or be comparable to the favored channels. For example, in SU(5) the rate for $n \to e^+\pi^-$ is twice that of $p \to e^+\pi^0$ [5]; however, the latter mode has a stronger experimental signature. It is conceivable that rates for channels with heavy nonstrange mesons (η, ρ, ω) are comparable in magnitude to those with pions [6]. In the lifetime limit where the expectation for any single channel is one event or less, searching in multiple decay modes enhances the chance that one observes any nucleon decay at all. Finally, observing proton decay from a nonstandard channel in the absence of a signal from $p \to e^+\pi^0$ might hint at some exotic scenario.

In this work, we describe nucleon decay searches for which the final state is comprised of two particles: a charged antilepton, e^+ or μ^+, and a nonstrange meson. These nucleon decays violate baryon number, B, but conserve baryon number minus lepton number, $B - L$. This paper, in combination with our recent publication searching for $p \to e^+\pi^0$ and $p \to \mu^+\pi^0$ [7], has covered all such two-body decay modes.

[*] Deceased.
[†] Also at Department of Physics and Astronomy, UCLA, CA 90095-1547, USA.
[‡] Also at BMCC/CUNY, Science Department, New York, New York, USA.

B. The Super-Kamiokande experiment

Super-Kamiokande is a large water Cherenkov detector located in the Kamioka mine under about 1 km rock overburden (2.7 km water equivalent) at the Ikenoyama mountain in Japan [8]. It is composed of a 39.3 m diameter by 41.4 m high vertical cylinder lined with 50-cm photomultiplier tubes (PMTs) facing the inner volume. The SK experiment has been collecting data since 1996 in four different experimental phases denoted as SK-I to SK-IV. The inner detector photo coverage is around 40% in SK-I, SK-III, and SK-IV but was 19% in SK-II. New front-end electronics called QBEE [9] were implemented in SK-IV, which enabled deadtime-free data acquisition of a wide time window of PMT hit information. This enabled neutron capture to be included in SK-IV analyses. The SK detector has been extensively tuned and calibrated [8].

Due to its large fiducial volume (22.5 kilotons, corresponding to about 7.5×10^{33} protons and 6.0×10^{33} neutrons), excellent event reconstruction performance [10] as well as long stable detector operation, SK has sensitivity to nucleon decay generally exceeding past experiments by an order of magnitude or more. Decays into a charged antilepton and a meson are particularly well suited for water Cherenkov detector searches since both the lepton and the meson or their decay particles are above the Cherenkov threshold and are visible in most cases.

The search for nucleon decay into a charged antilepton plus a meson using data from SK-I and SK-II (0.141 megaton · years) has been published previously [11]. Among those nucleon decay modes, the $p \to (e^+, \mu^+)\pi^0$ searches have been updated recently with additional data from SK-III and SK-IV along with several analysis improvements [7]. No evidence has been observed for any nucleon decays, and the corresponding lifetime limits were set for these channels.

In this work, we update the searches for proton decay into a charged antilepton (e^+, μ^+) plus a meson (η, ρ^0, ω) and neutron decay into a charged antilepton (e^+, μ^+) plus a meson (π^-, ρ^-) using the latest data set from SK-I to SK-IV, an exposure of 0.316 megaton · years.

C. Analysis improvements

This paper incorporates several major improvements in the analysis over the previously published results [11]. These improvements have already been implemented for $p \to e^+\pi^0$ and $p \to \mu^+\pi^0$ and recently published [7].

For some channels, the signal region in the reconstructed total momentum and invariant mass distribution parameters is separated into two distinct subregions ("boxes"), according to the total momentum. This permits a statistical separation of bound and free proton decays for channels that have good invariant mass and momentum resolution. For this paper, the channels that benefit are the $p \to l^+\eta$, $\eta \to 2\gamma$ searches ($l^+ = e^+, \mu^+$). The majority of the free proton decays have total momentum in the lower-momentum box, where the number of expected atmospheric neutrino background events is negligibly small. The two-box momentum separation is implemented for these channels in all data sets from SK-I to SK-IV. For more details see Sec. IV A.

Atmospheric neutrino background is often accompanied by neutron production whereas it is expected that nucleon decay seldom releases a free neutron [12]. For SK-IV analysis, a neutron capture reconstruction algorithm [13] is included, which allows us to reduce the atmospheric neutrino background rate. The neutron tagging is available, only for SK-IV, thanks to a triggerless readout scheme that records every hit in a wide time window. Following a primary event, we search over 435 μs for coincident hits near the vertex from the 2.2 MeV gamma ray from neutron capture on hydrogen, which occurs with a mean capture time of 200 μs in water. Description of the neutron simulation and the tagging algorithm can be found in Ref. [7]. In this analysis, the number of expected SK-IV background events is reduced using neutron tagging by 30–90% depending on the nucleon decay modes. A full summary of the resulting background for each SK period can be found in Table I.

The systematic uncertainties of the pion interactions in the oxygen nuclei and water have been reevaluated since the previous analysis of Ref. [11]. See Sec. V A for more details.

The new two-box strategy and neutron tagging provide better discovery reach. For example, the 3-σ discovery potential in the proton lifetime for $p \to e^+\eta$ search is estimated to be about 12% higher than the previous single-box analysis without neutron tagging for the exposure used in this analysis.

II. SIMULATION

A. Nucleon decay

Nucleon decay Monte Carlo (MC) samples are generated to determine the search strategy and to estimate the signal efficiencies. The MC simulation includes: initial nucleon decay kinematics, meson interactions in the oxygen nucleus for bound nucleon decays, hadron propagation in water, propagation of particles, and Cherenkov light emission, absorption, and scattering. The initial nucleon decay kinematics are identical to those in Ref. [11], while updated pion interactions and particle and Cherenkov light simulations in water are adopted from Ref. [7].

In the case of nucleon decay within the oxygen nucleus, the effects due to Fermi momentum, correlation with other nucleons [14] (correlated nucleon decay), nuclear binding energy, and meson-nucleon interactions are all taken into account [11]. The effective mass of the decayed neutron for $n \to e^+\pi^-$ MC is shown in Fig. 1. Unlike for the proton decay, there is no sharp peak at the neutron mass (940 MeV/c^2) because all the neutrons in a H_2O molecule are bound in a nucleus and there is no free neutron decay.

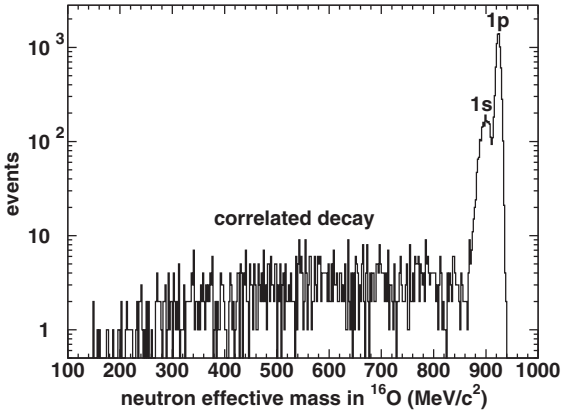

FIG. 1. The effective mass of the decayed neutron in ^{16}O for $n \to e^+\pi^-$ as simulated by Monte Carlo.

The largest and most energetic peak corresponds to the $1p$ state; the $1s$ state is nearby. The nuclear binding energies are 39.0 MeV for the $1s$ state and 15.5 MeV for the $1p$ state [15]. Correlated neutron decay, which accounts for the possibility of another nucleon recoiling with the decaying nucleon, makes the tail in the lower mass region.

The meson-nucleon interactions in an oxygen nucleus are simulated with the NEUT neutrino interaction simulation [16]. Mesons generated in an oxygen nucleus may interact with nucleons before they escape from the nucleus. The position of the nucleon decay in a nucleus is determined by the Woods-Saxon nuclear density distribution in the simulation. From this position, π, η, and ω mesons are tracked within the oxygen nucleus. The lifetime of the ρ meson is short enough ($\beta\gamma c\tau \sim 0.3$ fm) that it decays immediately inside the nucleus into two π mesons. Therefore, the nuclear effects of the ρ meson itself are not considered in the simulation, but those of the secondary pions are included.

The pion interaction model in NEUT is a semiclassical cascade model. The interaction probabilities (mean free paths) for low-momentum pions are calculated with the Delta-hole model by Oset *et al.* [17]. The pion interaction probabilities for high-momentum pions are extracted from the $\pi^{\pm}$-nucleus scattering experimental data. All the pion interaction probabilities and cross section parameters have been tuned with various $\pi^{\pm}$-nucleus scattering data, including C, O, Al, Fe [7], since the previous paper [11]. Figure 2 shows the π^- cross sections of the external data and MC on ^{12}C [18]. The tuned MC used in this analysis increased the cross sections with the largest improvement at around 500 MeV/c.

The interactions between the η and nucleons in the nucleus are considered through a baryon resonance of $N(1535)$ and the corresponding cross section is calculated by the Breit-Wigner formula. Since pions can be generated by the decay of the resonance, nuclear effects for them are considered. Figure 3 shows the fractions of the meson interactions in the oxygen nucleus in the $p \to e^+\eta$ MC.

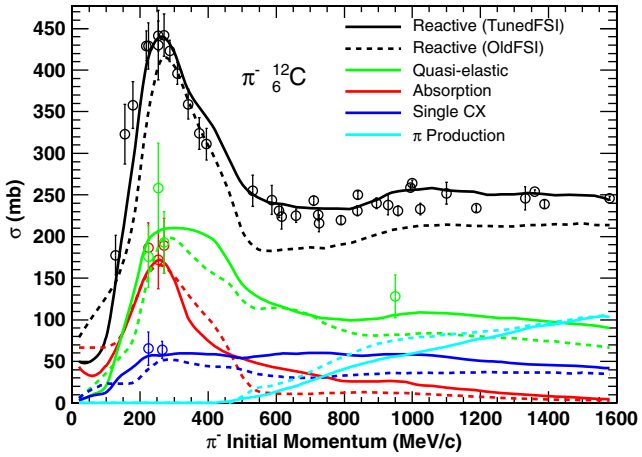

FIG. 2. The π^- interaction cross section on ^{12}C as a function of momentum. Open circles indicate existing data [18]; dashed and solid lines show before and after the tune, respectively. The colors correspond to the total cross section and exclusive channels: total (black), quasielastic scattering (green), absorption (red), charge exchange "CX" (blue), and π production (light blue). "FSI" stands for final state interaction.

The ω meson interactions with a nucleon in an oxygen nucleus are calculated with a boson exchange model [19].

Uncertainties due to these physics processes are taken into account within the systematic error estimations on the signal efficiencies as discussed in Sec. VA.

B. Atmospheric neutrinos

The background for nucleon decay searches comes from atmospheric neutrino interactions in water. The standard Super-Kamiokande atmospheric neutrino simulations [16,20–22] are used to estimate the background rate.

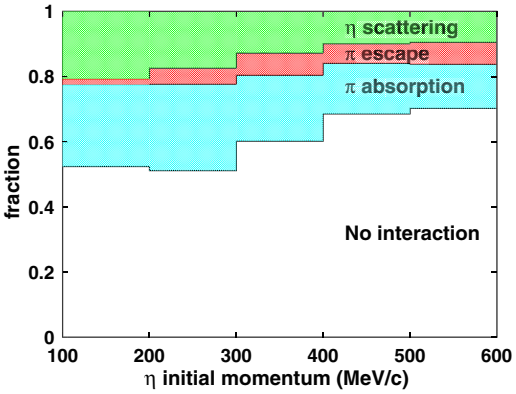

FIG. 3. Fraction of meson interactions in the oxygen nucleus in bins of η momentum generated by $p \to e^+\eta$ MC. η's that exit the nucleus without experiencing any interactions are indicated by the portion labeled "No interaction." If at least one of the pions generated via the baryon resonance of $N(1535)$ is absorbed, it is called "π absorption." If none of the pions are absorbed, it is called "π escape."

The model includes an atmospheric neutrino flux calculation, neutrino oscillation, and a detailed model of neutrino-nucleus interaction cross sections. The meson interactions in the oxygen nucleus are treated similarly for the nucleon decay and the atmospheric neutrino MC. Simulated data samples equivalent to around 500 years of detector exposure are generated for each SK period. The detector simulation, including Cherenkov light production, scattering, absorption, and detector response, is identical for the nucleon decay signal MC and the atmospheric neutrino background MC.

Uncertainties of the neutrino flux, neutrino cross sections, pion-nuclear interactions as well as hadron propagation in water are all taken into account in the systematic error estimates on the number of the expected background events as discussed in Sec. VA.

The neutrino and the pion interactions in the atmospheric neutrino background for the $p \to e^+\pi^0$ search in SK were experimentally validated using an accelerator neutrino beam and a 1-kiloton water Cherenkov detector [23]. The dynamics of pion production and interactions relevant for the nucleon decay searches for the SK-type water Cherenkov detector have been verified.

III. DATA REDUCTION AND RECONSTRUCTION

Data from 91.5, 49.1, 31.8, and 143.8 kiloton · year exposures, corresponding to the 1489.2, 798.2, 518.1, and 2339.4 live days of the experiment during the SK-I, SK-II, SK-III, and SK-IV phases, are used. Several stages of reduction are applied to suppress the cosmic ray muon background and prepare samples for the physics analyses. The reduction algorithms are identical to those used for atmospheric neutrino analyses and nucleon decay searches [24].

Fully contained (FC) events are selected by requiring a vertex inside of the 22.5 kiloton fiducial volume (2 m away from the inner detector wall), visible energy greater than 30 MeV, and no hit-PMT clusters in the outer detector.

Event reconstruction algorithms are applied to all of the FC events to determine the event vertex location, find Cherenkov ring directions, assign a particle identification of showering or nonshowering to each ring, assign particle momentum to each ring, and identify muon decay electrons that follow the primary event by microseconds. The same reconstruction algorithms are applied to both the observed data and the MCs. The algorithms are the same as for atmospheric neutrino analyses, with the details of their algorithms described in [10].

One of the most important event reconstructions for nucleon decay searches is the energy scale because we distinguish the nucleon decay events from the atmospheric neutrino background events using their invariant mass and momentum. The energy scale uncertainty is estimated by taking the absolute scale difference between control sample data and MC as well as the time variation of control sample data for each SK period. For the four SK periods, the energy scale uncertainties are 1.1%, 1.7%, 2.7%, and 2.1% for SK-I, SK-II, SK-III, and SK-IV, respectively. The uncertainties from SK-I to SK-III are same as in a previous publication [25] and details of the energy reconstruction and the error estimation can be found there. Figure 4 shows the reconstructed π^0 mass distributions used in the absolute energy scale error estimation of SK-IV. Good agreement is observed between data and MC in reconstruction of the π^0 mass. Zenith angle-dependent nonuniformities of the energy scale are 0.6%, 0.6%, 1.3%, and 0.7% for SK-I, SK-II, SK-III, and SK-IV, respectively. These energy scale errors are used in the systematic error estimations described in Sec. VA.

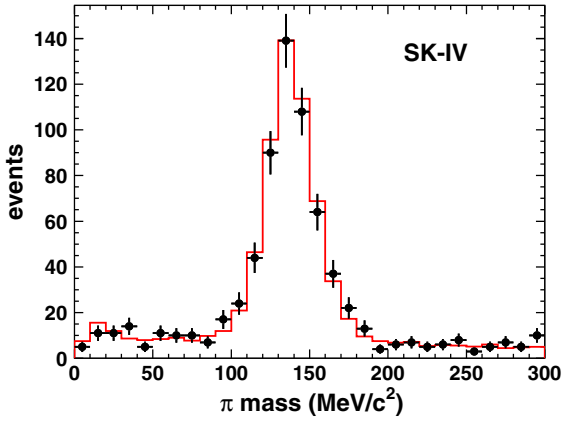

FIG. 4. Reconstructed invariant mass distribution of the atmospheric-neutrino-induced π^0 events in the observed data (black dot) and the atmospheric neutrino MC samples (red histogram) used in the absolute energy scale error estimation in SK-IV. MC events are normalized by the live time of the observed data (1631 days).

The reconstructed total momentum, $P_{\rm tot}$, the total energy $E_{\rm tot}$, and the invariant mass $M_{\rm tot}$ are defined as

$$P_{\rm tot} = \left| \sum_i^{\rm all} \vec{p}_i \right|, \tag{1}$$

$$E_{\rm tot} = \sum_i^{\rm all} \sqrt{|\vec{p}_i|^2 + m_i^2}, \tag{2}$$

$$M_{\rm tot} = \sqrt{E_{\rm tot}^2 - P_{\rm tot}^2}, \tag{3}$$

where $\vec{p}_i$ is the momentum of each Cherenkov ring and m_i is the mass of a particle.

The meson mass is reconstructed in a similar way by summing up the momenta and energies of the secondary particles from the meson decay. Under the assumption of a particular meson decay, the meson mass is calculated for all possible combinations of particle type assignment and the best combination in which the reconstructed mass is the closest to the expected mass is selected.

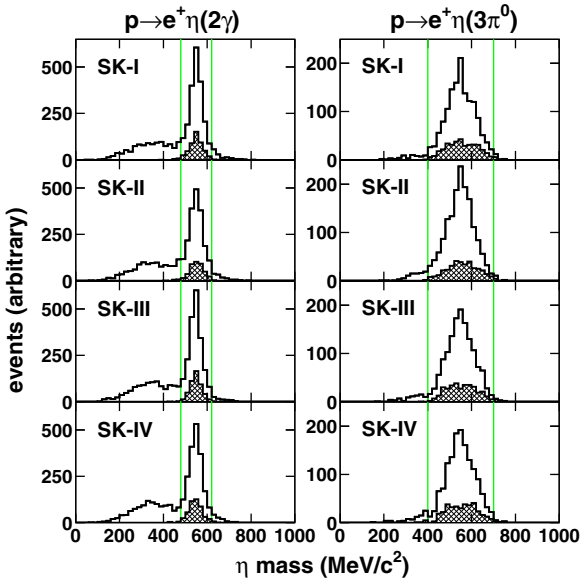

FIG. 5. The reconstructed η mass distributions for $p \to e^+\eta$ MC events for $\eta \to 2\gamma$ search (left) and $\eta \to 3\pi^0$ (right) search for each SK period. The histograms show all simulated $p \to e^+\eta$ events. For the left plots the eta meson is reconstructed under the assumption of $\eta \to 2\gamma$, and for the right plots the eta meson is reconstructed under the assumption of $\eta \to 3\pi^0$. The hatched histograms show, for free proton decays, the true $\eta \to 2\gamma$ events (left) and true $\eta \to 3\pi^0$ events (right). The event selections (A1–A2) of Sec. IV A are applied. The inside of the two vertical green lines corresponds to the signal region.

For example, Fig. 5 shows the reconstructed η mass distributions for the $p \to e^+\eta$ MC events for each SK period. The η mass is reconstructed well. The open histogram contains all the relevant η decay channels associated with the signal MC. For example, the broad peak between 200–400 MeV/c^2 in the left plots is from all the η decays except for $\eta \to 2\gamma$. The mass resolution is observed to be worse for the $3\pi^0$ search since there are six true gamma rays in the final state, but only up to four or five Cherenkov rings are reconstructed; the ring-counting algorithm terminates at five rings. For both meson decay searches, there is no significant difference in the mass reconstruction among the four SK periods. Details of the comparison of event reconstructions between SK-I and SK-II are found in the previous publication [11].

IV. EVENT SELECTION

The event selections were already optimized in the previous analysis [11] for each nucleon decay mode to maximize the lifetime sensitivity and are exactly the same in this analysis except when the two-box total momentum separation and the SK-IV neutron tagging are used.

The event selections for each nucleon decay ($l^+ = e^+$, μ^+) search are described in the following subsections. The signal selection efficiency and the number of expected atmospheric neutrino backgrounds, as well as the observed data for each nucleon decay search and each SK period, are summarized in Table I.

A. $p \to l^+\eta$ search

The η meson, with a mass of 548 MeV/c^2 and a lifetime of 5×10^{-19} seconds, has three dominant decay modes. Two of them, $\eta \to 2\gamma$ (branching ratio = 39%) and $\eta \to 3\pi^0$ (branching ratio = 33%), are analyzed. The $\eta \to \pi^+\pi^-\pi^0$ (branching ratio = 23%) is not used because the branching ratio is smaller and the signal selection efficiency is worse [11].

1. $\eta \to 2\gamma$ search

The following event selection is used:

(A1) the number of Cherenkov rings is three,
(A2) all the rings are shower-type rings for $p \to e^+\eta$ and one of the rings is a nonshower-type ring for $p \to \mu^+\eta$,
(A3) the invariant mass is between 480 and 620 MeV/c^2,
(A4) the number of Michel electrons is 0 for $p \to e^+\eta$ or 1 for $p \to \mu^+\eta$,
(A5) the total momentum is less than 250 MeV/c and the invariant mass is between 800 and 1050 MeV/c^2,
(A6) the total momentum is greater than or (A7) less than 100 MeV/c (total momentum separation),
(A8) the number of neutrons is 0 for the upper or (A9) lower total momentum region in SK-IV.

After the selections (A1–A5), the total momentum separation (A6–A7) into two search boxes is implemented since the following three extra criteria are satisfied in the lower-momentum signal box: (1) the expected number of the background events is negligibly small ($\ll$0.1 events for each SK period), (2) the signal efficiency is sufficiently high (>1%), (3) most of the free proton decays are in this region.

The signal selection efficiency and the number of expected background events at each event selection step are shown in Fig. 6. The event selection by total momentum and invariant mass at selection (A5) significantly reduces the atmospheric neutrino background. The total expected number of the background is further reduced and becomes negligibly small, ~0.03 (<0.01) integrated over all the SK periods for $p \to e^+\eta$ ($p \to \mu^+\eta$) search (see Table I for detail), in the lower signal box at selection (A7). The signal efficiency is still sufficiently high (>1%) in the lower box.

The total mass and total momentum distributions are shown in Figs. 7 and 8. Most of the free protons decay in the lower box (total momentum < 100 MeV/c) for the $\eta \to 2\gamma$ searches shown in the upper-left two plots, and the data and the atmospheric neutrino MC agree with each other in all the lower plots in Fig. 8.

2. $\eta \to 3\pi^0$ search

The following event selection is used:

(B1) the number of Cherenkov rings is four or five,

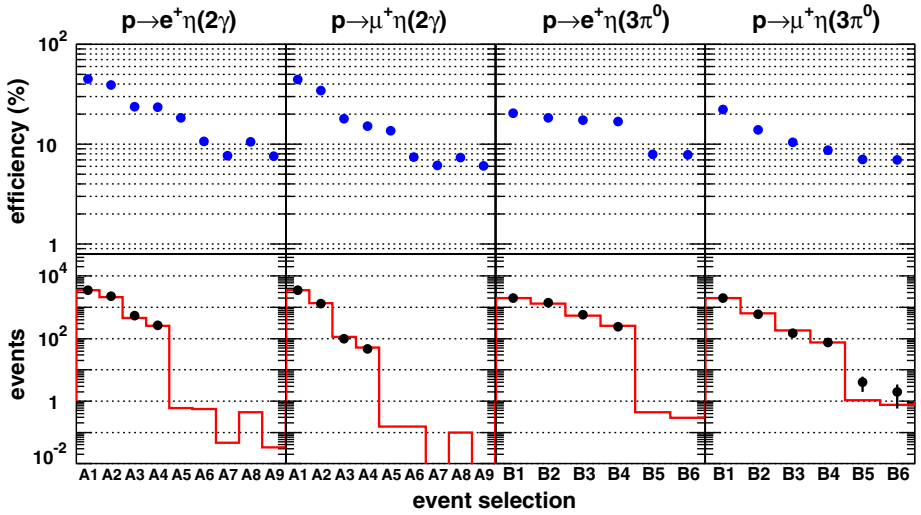

FIG. 6. The signal efficiencies (upper) and the number of expected backgrounds (lower, red histogram) and data candidates (lower, black dots) for $p \to e^+\eta$ ($\eta \to 2\gamma$), $p \to \mu^+\eta$ ($\eta \to 2\gamma$), $p \to e^+\eta$ ($\eta \to 3\pi^0$), and $p \to \mu^+\eta$ ($\eta \to 3\pi^0$) searches from left to right. The results from SK-I to SK-IV are combined. The event selection is defined in the text.

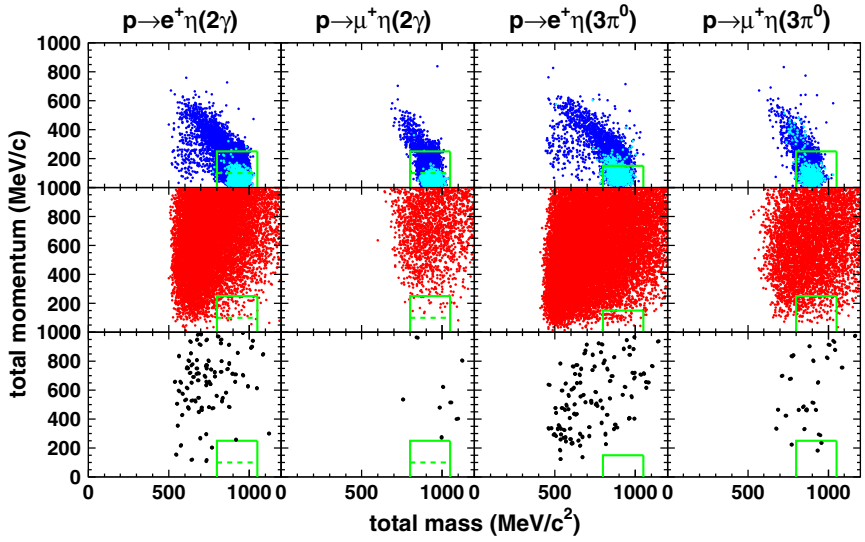

FIG. 7. Total invariant mass and total momentum for $p \to l^+\eta$ MC (top, cyan for free proton and blue for bound proton), atmospheric neutrino background MC corresponding to about 2000 years live time of SK (middle), and data (bottom) for $p \to e^+\eta$ ($\eta \to 2\gamma$), $p \to \mu^+\eta$ ($\eta \to 2\gamma$), $p \to e^+\eta$ ($\eta \to 3\pi^0$), and $p \to \mu^+\eta$ ($\eta \to 3\pi^0$) searches from left to right. All the event selections except (A5–A7) and (B5) in Sec. IV A are applied. The results from SK-I to SK-IV are combined. The signal box is shown as a green box. For the $p \to l^+\eta$ (2γ) searches, the total momentum is separated at the horizontal dashed line in the signal box.

(B2) all the rings are shower-type rings for $p \to e^+\eta$ and one of the rings is a nonshower-type ring for $p \to \mu^+\eta$,
(B3) the η mass is between 400 and 700 MeV/c^2,
(B4) the number of Michel electrons is 0 for $p \to e^+\eta$ and 1 for $p \to \mu^+\eta$,
(B5) the total momentum is less than 150 MeV/c for $p \to e^+\eta$ and less than 250 MeV/c for $p \to \mu^+\eta$; the total invariant mass is between 800 and 1050 MeV/c^2,
(B6) the number of neutrons is 0 in SK-IV.

The signal selection efficiency and the number of expected background events at each event selection step are shown in Fig. 6. The total mass and total momentum distributions are shown in Figs. 7 and 8. Unlike the $\eta \to 2\gamma$ mode, a significant fraction of the events have reconstructed total momentum greater than 100 MeV/c even for free proton decay. Therefore, we do not implement the two-box total momentum separation.

After the full event selection in the $p \to \mu^+\eta$ search has been applied, there are two data candidates remaining, one in SK-II and another in SK-IV. The total number of expected background events integrated over all the meson decay modes and all SK periods is 0.85. The Poisson

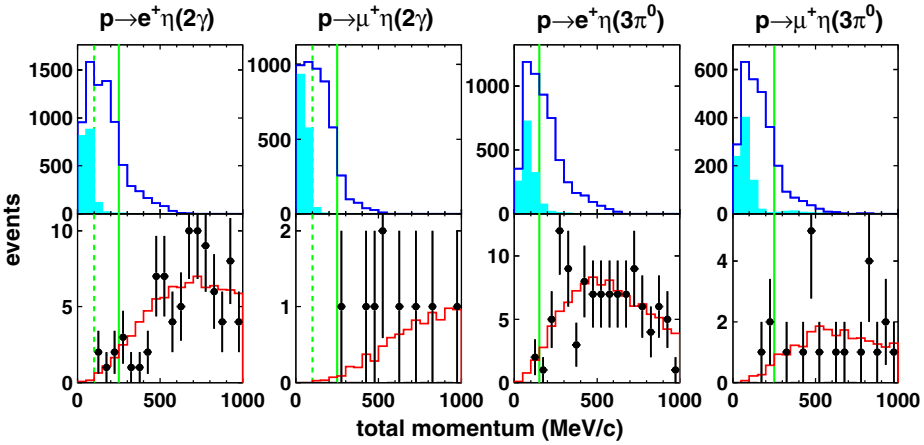

FIG. 8. Total momentum for $p \to l^+\eta$ MC (upper, open histogram for bounded protons and shaded histogram for free protons), atmospheric neutrino MC (lower, red histogram), and data (lower, black circles) for $p \to e^+\eta$ ($\eta \to 2\gamma$), $p \to \mu^+\eta$ ($\eta \to 2\gamma$), $p \to e^+\eta$ ($\eta \to 3\pi^0$), and $p \to \mu^+\eta$ ($\eta \to 3\pi^0$) searches from left to right. All the event selections except (A5–A7) and (B5) in Sec. IV A are applied. The atmospheric neutrino MC is normalized to data by area. Results from SK-I to SK-IV are combined. The signal region corresponds to the left side from the vertical green solid line. The vertical dashed line for $p \to l^+\eta$ (2γ) corresponds to the total momentum separation cut value. Total momenta for the $p \to \mu^+\eta$ ($\eta \to 3\pi^0$) data candidates are 188 MeV/c and 239 MeV/c.

probability to observe two or more events is 20.9%, as summarized in Table III.

The data candidate found in SK-II using the current analysis was also found in the previously published analysis. The previous work also found an additional data candidate in SK-II. In that event, a faint nonshowerlike ring reconstructed in the previous analysis is not reconstructed in this work, excluding it from the selection criteria. Event reconstruction improvements, such as tuning of the backward charge within the charge separation algorithm among Cherenkov rings, can cause such changes in the ring counting outcome on an event-by-event basis.

B. $p \to l^+\rho^0$

The ρ^0 meson, with a mass of 775 MeV/c^2 and a width of 149 MeV, decays immediately into $\pi^+\pi^-$ with a branching ratio of nearly 100%.

The following event selection is used for this search:

(C1) the number of Cherenkov rings is three,
(C2) one of the rings is a shower-type ring for $p \to e^+\rho^0$ and all the rings are nonshower-type rings for $p \to \mu^+\rho^0$,
(C3) the ρ^0 mass is between 600 and 900 MeV/c^2,
(C4) the number of Michel electrons is 0 or 1 for $p \to e^+\rho^0$ and 1 or 2 for $p \to \mu^+\rho^0$,
(C5) the total momentum is less than 150 MeV/c for $p \to e^+\rho^0$ and less than 250 MeV/c for $p \to \mu^+\rho^0$; the total invariant mass is between 800 and 1050 MeV/c^2,
(C6) the number of neutrons is 0 in SK-IV.

Figure 9 shows the signal selection efficiency and the number of expected background events at each event selection step. The total invariant mass and momentum distributions are shown in Figs. 10 and 11.

There are two data candidates in SK-IV for the $p \to e^+\rho^0$ search and one candidate in SK-I for the $p \to \mu^+\rho^0$ search. The SK-I event was also selected in the analysis of the previous publication. The total number of expected background events is 0.64 for $p \to e^+\rho^0$ and 1.30 for $p \to \mu^+\rho^0$ searches.

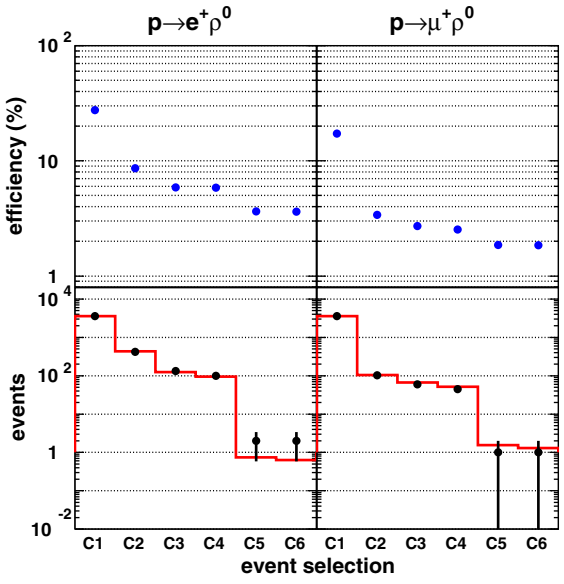

FIG. 9. The signal efficiencies (upper) and the number of expected backgrounds (lower, red histogram) and data candidates (lower, black dots) for $p \to e^+\rho^0$ (left) and $p \to \mu^+\rho^0$ (right) searches. The results from SK-I to SK-IV are combined. The event selection is defined in the text.

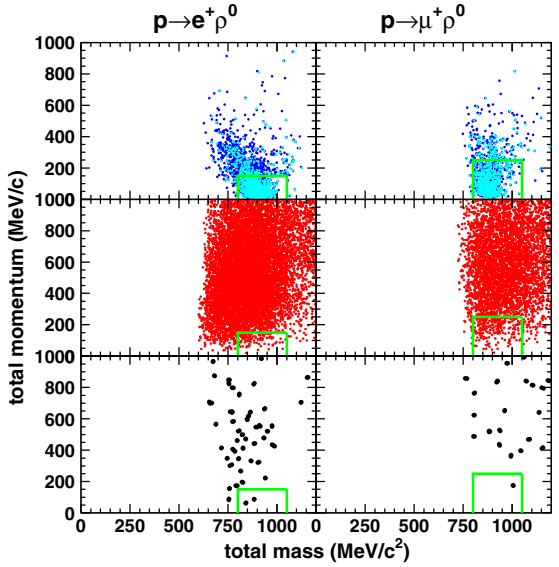

FIG. 10. Total invariant mass and total momentum for $p \to l^+\rho^0$ MC (top, cyan for free proton and blue for bound proton), atmospheric neutrino background MC corresponding to about 2000 years live time of SK (middle), and data (bottom) for $p \to e^+\rho^0$ (left) and $p \to \mu^+\rho^0$ (right) searches. All the event selections except (C5) in Sec. IV B are applied. The results from SK-I to SK-IV are combined. The signal box is shown as a green box.

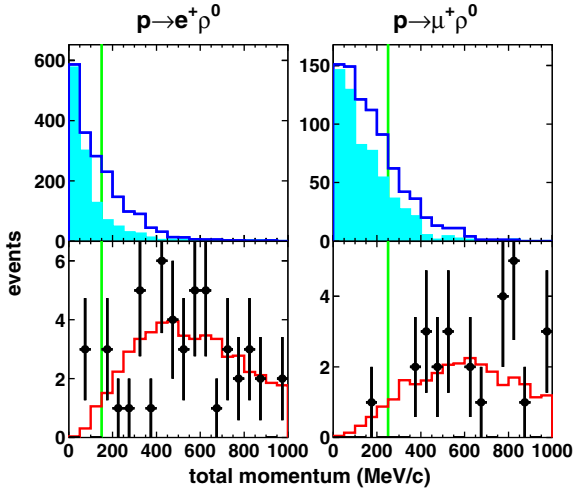

FIG. 11. Total momentum for $p \to l^+\rho^0$ MC (upper, open histogram for bounded protons and shaded histogram for free protons), atmospheric neutrino MC (lower, red histogram), and data (lower, black circles) for $p \to e^+\rho^0$ (left) and $p \to \mu^+\rho^0$ (right) searches. All the event selections except (C5) in Sec. IV B are applied. The atmospheric neutrino MC is normalized to data by area. Results from SK-I to SK-IV are combined. The signal region corresponds to left side from the vertical green line. Total momenta are 61 MeV/c and 90 MeV/c for the $p \to e^+\rho^0$ data candidates and 179 MeV/c for the $p \to \mu^+\rho^0$ data candidate.

C. $p \to l^+\omega$

The ω meson has a mass of 783 MeV/c^2 and immediately decays due to a width of 8.5 MeV. Two decay modes are analyzed: one is the $\omega \to \pi^+\pi^-\pi^0$ mode (branching ratio = 89%), and the other is the $\omega \to \pi^0\gamma$ mode (branching ratio = 8%).

1. $\omega \to \pi^0\gamma$ search

The following event selection is used for this search:

(D1) the number of Cherenkov rings is 3 or 4 for $p \to e^+\omega$ and 2 or 3 for $p \to \mu^+\omega$,
(D2) all rings are shower-type rings,
(D3) the ω mass is between 650 and 900 MeV/c^2,
(D4) the number of Michel electrons is 0 for $p \to e^+\omega$ and 1 for $p \to \mu^+\omega$,
(D5) the total momentum is less than 150 MeV/c for $p \to e^+\omega$ and less than 200 MeV/c for $p \to \mu^+\omega$; the invariant mass is between 800 and 1050 MeV/c^2 for $p \to e^+\omega$,
(D6) the number of neutrons is 0 in SK-IV.

For the $p \to \mu^+\omega$ mode, the muon momentum is lower than the Cherenkov threshold and the muon ring is not observed.

Figure 12 shows the signal selection efficiency and the number of expected background events at each event selection step. The total mass and total momentum distributions are shown in Figs. 13 and 14.

2. $\omega \to \pi^+\pi^-\pi^0$ search

The following event selection is used for this search:

(E1) the number of Cherenkov rings is 4 for $p \to e^+\omega$ and 3 for $p \to \mu^+\omega$,
(E2) one of the rings is a nonshower ring,
(E3) the π^0 mass is between 85 and 185 MeV/c^2,
(E4) the number of Michel electrons is 0 or 1 for $p \to e^+\omega$ and 2 for $p \to \mu^+\omega$,
(E5) the total momentum is less than 200 MeV/c, and the total invariant mass is between 600 and 800 MeV/c^2 for $p \to e^+\omega$ and between 450 and 700 MeV/c^2 for $p \to \mu^+\omega$,
(E6) the positron momentum is between 100 and 200 MeV/c for $p \to e^+\omega$,
(E7) the number of neutrons is 0 in SK-IV.

Due to the strong interaction of the charged pions in water, finding both charged pion rings is difficult. Therefore, we require finding only one of the two charged pion rings in these searches. Since one of the two charged pions is assumed to be invisible in the selection criteria, the invariant mass for the ω can not be reconstructed. Instead, we require that the reconstructed π^0 invariant mass is consistent with the π^0 mass. In order to reduce the background even further, the positron momentum is also required to be consistent with the expected positron momentum for the $p \to e^+\omega$ mode. The positron momentum distribution is shown in Fig. 15.

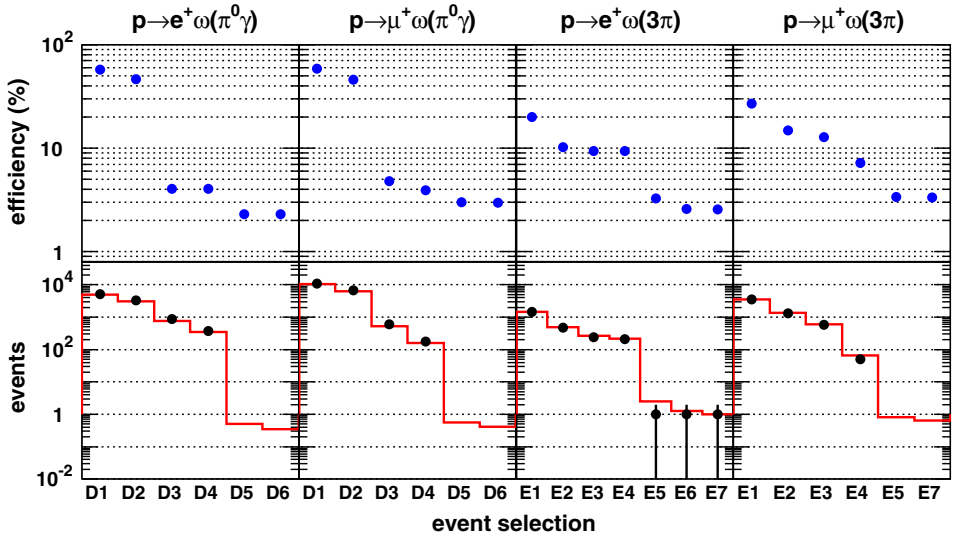

FIG. 12. The signal efficiencies (upper) and the number of expected backgrounds (lower, red histogram) and data candidates (lower, black dots) for $p \to e^+\omega\,(\omega \to \pi^0\gamma)$, $p \to \mu^+\omega\,(\omega \to \pi^0\gamma)$, $p \to e^+\omega\,(\omega \to 3\pi)$, and $p \to \mu^+\omega\,(\omega \to 3\pi)$ searches from left to right. The results from SK-I to SK-IV are combined. The event selection is defined in the text.

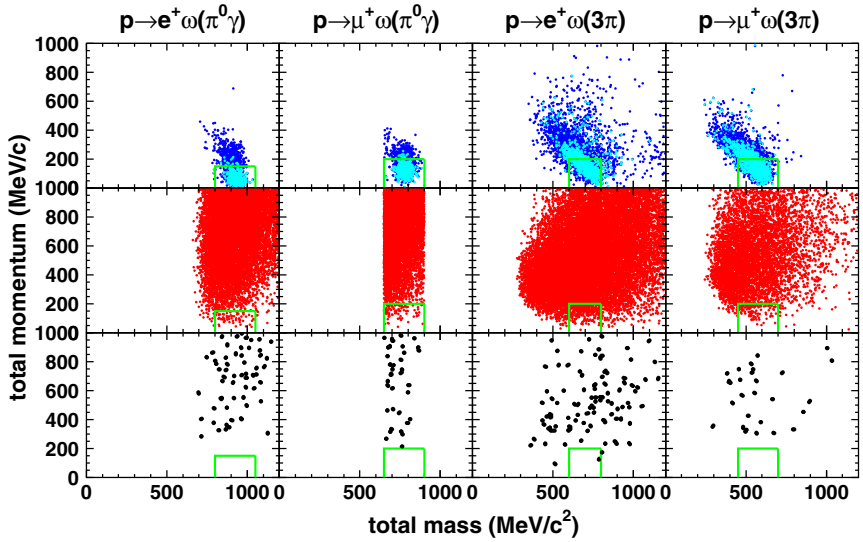

FIG. 13. Total invariant mass and total momentum for $p \to l^+\omega$ MC (top, cyan for free proton and blue for bound proton), atmospheric neutrino background MC corresponding to about 2000 years live time of SK (middle), and data (bottom) for $p \to e^+\omega\,(\omega \to \pi^0\gamma)$, $p \to \mu^+\omega\,(\omega \to \pi^0\gamma)$, $p \to e^+\omega\,(\omega \to 3\pi^0)$, and $p \to \mu^+\omega\,(\omega \to 3\pi^0)$ searches from left to right. All the event selections except (D5) and (E5) in Sec. IV C are applied. The results from SK-I to SK-IV are combined. The signal box is shown as a green box.

There is one data candidate in SK-I for $p \to e^+\omega$ search and the number of total expected background events is 1.35. An identical event was selected in the previous analysis.

D. $n \to l^+\pi^-$

The following event selection is used for this search:

(F1) the number of Cherenkov rings is two,

(F2) one of the rings is a shower-type ring for $n \to e^+\pi^-$ and all the rings are nonshower-type rings for $n \to \mu^+\pi^-$,

(F3) the number of Michel electrons is 0 for $n \to e^+\pi^-$ and 1 for $n \to \mu^+\pi^-$,

(F4) the total momentum is less than 250 MeV/c, and the total invariant mass is between 800 and 1050 MeV/c^2,

(F5) the number of neutrons is 0 in SK-IV.

In these modes, a Cherenkov ring from the charged pion generated from the nucleon decay can be directly observed. It is not necessary to select the events by a meson invariant mass for these modes.

Figure 16 shows the signal selection efficiency and the number of expected background events at each event

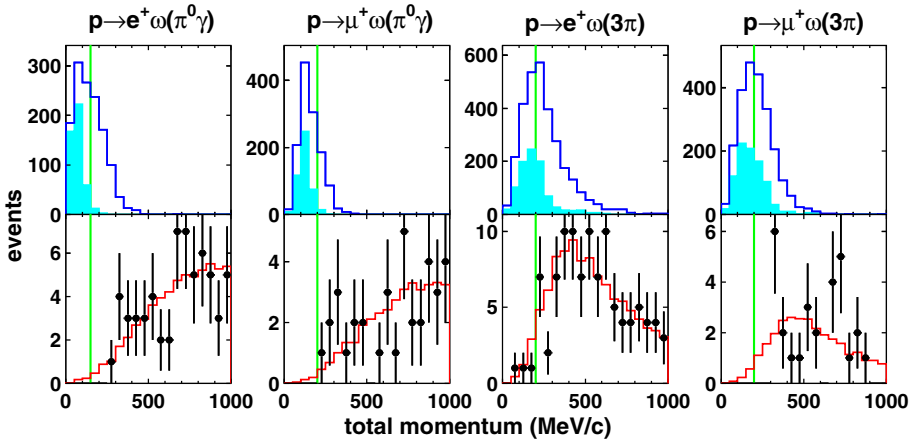

FIG. 14. Total momentum for $p \to l^+\omega$ MC (upper, open histogram for bounded protons and shaded histogram for free protons), atmospheric neutrino MC (lower, red histogram), and data (lower, black circles) for $p \to e^+\omega$ ($\omega \to \pi^0\gamma$), $p \to \mu^+\omega$ ($\omega \to \pi^0\gamma$), $p \to e^+\omega$ ($\omega \to 3\pi$), and $p \to \mu^+\omega$ ($\omega \to 3\pi$) searches from left to right. All the event selections except (D5) and (E5) in Sec. IV C are applied. The atmospheric neutrino MC is normalized to data by area. Results from SK-I to SK-IV are combined. The signal region corresponds to the left side from the vertical green line. Total momentum for $p \to e^+\omega$ ($\omega \to 3\pi$) data candidate is 124 MeV/c.

selection step. The total mass and total momentum distributions are shown in Figs. 17 and 18.

There is one data candidate in SK-III in $n \to \mu^+\pi^-$ search and the number of total expected background events is 0.77.

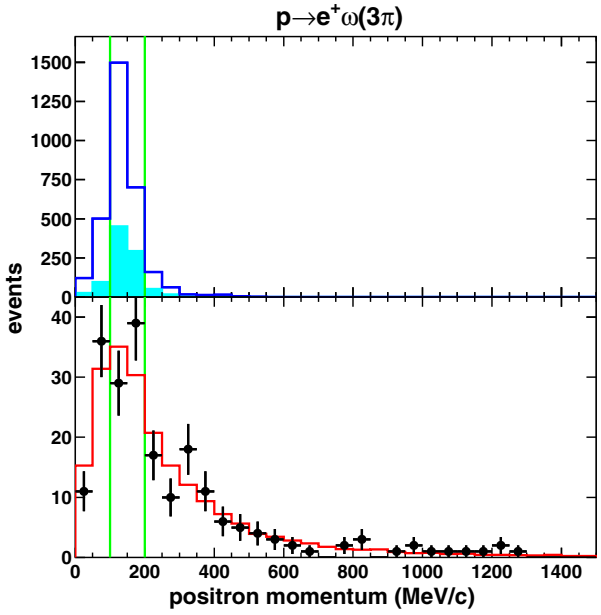

FIG. 15. Positron momentum for $p \to e^+\omega$ MC (upper, open histogram for bounded protons and shaded histogram for free protons), atmospheric neutrino MC (lower, red histogram), and data (lower, black circles) for $p \to e^+\omega$ ($\omega \to 3\pi$) search. The event selections (E1–E4) of Sec. IV C are applied. The atmospheric neutrino MC is normalized to data by area. Results from SK-I to SK-IV are combined. The inside of the two vertical green lines corresponds to the signal region.

In the previous published analysis, there was one data candidate in SK-I for the $n \to \mu^+\pi^-$ search. In both previous and current analyses, the event vertex is in the fiducial volume, the number of rings is two, both rings are nonshower types, and the number of Michel electrons is one, passing those selection criteria. The invariant mass and momentum, ($M_{\rm tot}$, $P_{\rm tot}$) was (809 MeV/c^2, 245 MeV/c) in the previous analysis but changed slightly to (829 MeV/c^2, 253 MeV/c) in this analysis. The $P_{\rm tot}$ is near the signal box

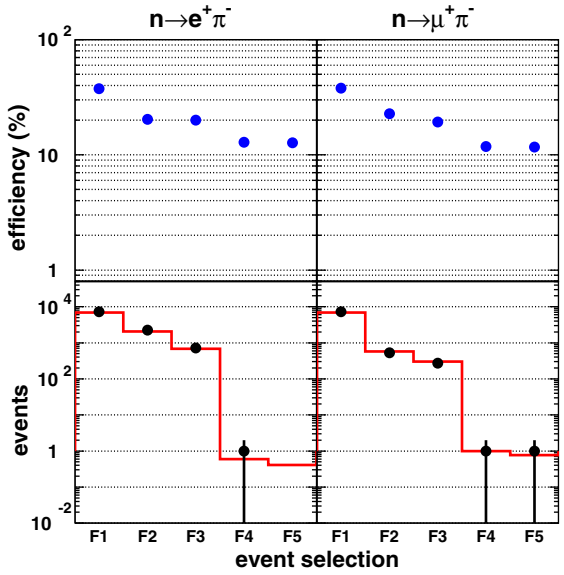

FIG. 16. The signal efficiencies (upper) and the number of expected background events (lower, red histogram) and data candidates (lower, black dots) for $n \to e^+\pi^-$ (left) and $n \to \mu^+\pi^-$ (right) searches. The results from SK-I to SK-IV are combined. The event selection is defined in the text.

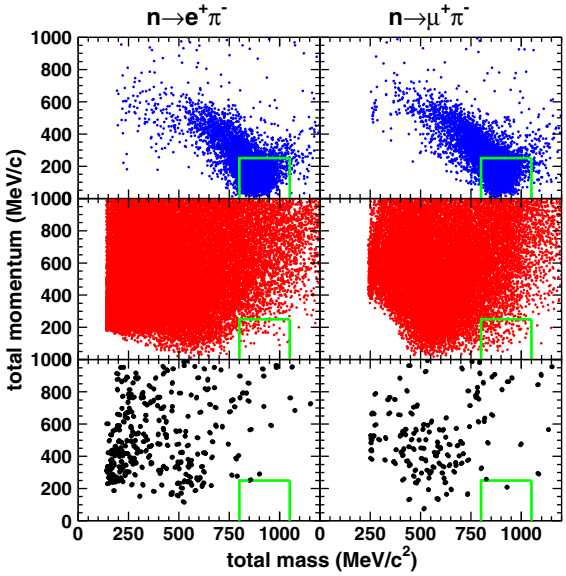

FIG. 17. Total invariant mass and total momentum for $n \to l^+\pi^-$ MC (top), atmospheric neutrino background MC corresponding to about 2000 years live time of SK (middle), and data (bottom) for $n \to e^+\pi^-$ (left) and $n \to \mu^+\pi^-$ (right) searches. All the event selections except (F4) in Sec. IV D are applied. The results from SK-I to SK-IV are combined. The signal box is shown as a green box.

but above the cut threshold (250 MeV/c) and this event fails final selection for this analysis.

E. $n \to l^+\rho^-$

The ρ^- meson has a mass of 770 MeV/c^2 and a width of 150 MeV, immediately decaying into $\pi^-\pi^0$ with a branching ratio of nearly 100%.

The following event selection is used for this search:

(G1) the number of Cherenkov rings is four for $n \to e^+\rho^-$ and three for $n \to \mu^+\rho^-$,
(G2) one of the rings is a nonshower ring,
(G3) the ρ^- mass is between 600 and 900 MeV/c^2,
(G4) the π^0 mass is between 85 and 185 MeV/c^2,
(G5) the number of Michel electrons is 0 for $n \to e^+\rho^-$ and 1 for $n \to \mu^+\rho^-$,
(G6) the total momentum is less than 250 MeV/c for $n \to e^+\rho^-$ and less than 150 MeV/c for $n \to \mu^+\rho^-$; the total invariant mass is between 800 and 1050 MeV/c^2 for $n \to e^+\rho^-$,
(G7) the number of neutrons is 0 in SK-IV.

The tighter total momentum cut of $P_{\rm tot} < 150$ MeV/c is applied to reduce the background for the $n \to \mu^+\rho^-$ mode because the nucleon invariant mass cannot be reconstructed for the mode due to the invisible muon.

Figure 19 shows the signal selection efficiency and the number of expected background events at each event selection step. The total mass and total momentum distributions are shown in Figs. 20 and 21.

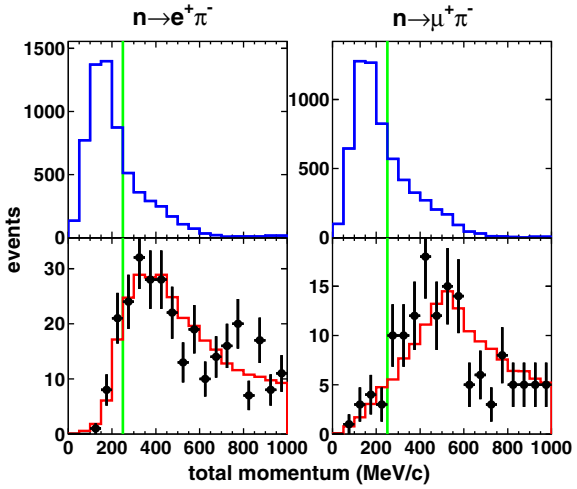

FIG. 18. Total momentum for $n \to l^+\pi^-$ MC (upper), atmospheric neutrino MC (lower, red histogram), and data (lower, black circles) for $n \to e^+\pi^-$ (left) and $n \to \mu^+\pi^-$ (right) searches. All the event selections except (F4) in Sec. IV D are applied. The atmospheric neutrino MC is normalized to data by area. Results from SK-I to SK-IV are combined. The signal region corresponds to the left side from the vertical green line. Total momentum for $n \to \mu^+\pi^-$ data candidate is 205 MeV/c.

There are four data candidates (one in SK-I, one in SK-II, and two in SK-III) in the $n \to e^+\rho^-$ search and one data candidate in SK-II in the $n \to \mu^+\rho^-$ search. The number of total expected background events is 0.87 for $n \to e^+\rho^-$ and 0.96 for $n \to \mu^+\rho^-$ searches. The Poisson probability to observe four or more events is

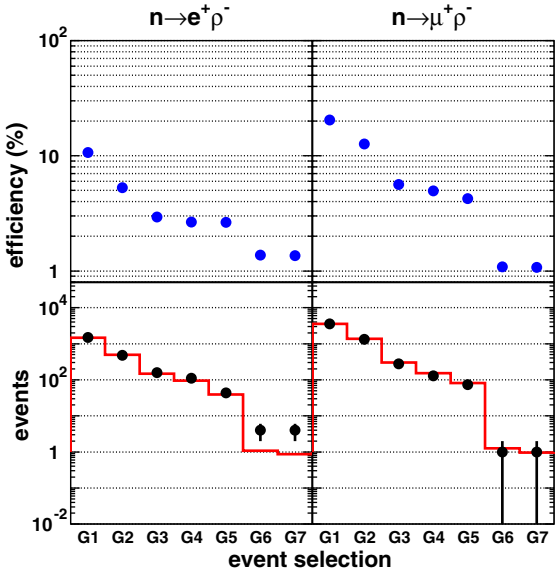

FIG. 19. The signal efficiencies (upper) and the number of expected backgrounds (lower, red histogram) and data candidates (lower, black dots) for $n \to e^+\rho^-$ (left) and $n \to \mu^+\rho^-$ (right). The results from SK-I to SK-IV are combined. The event selection is defined in the text.

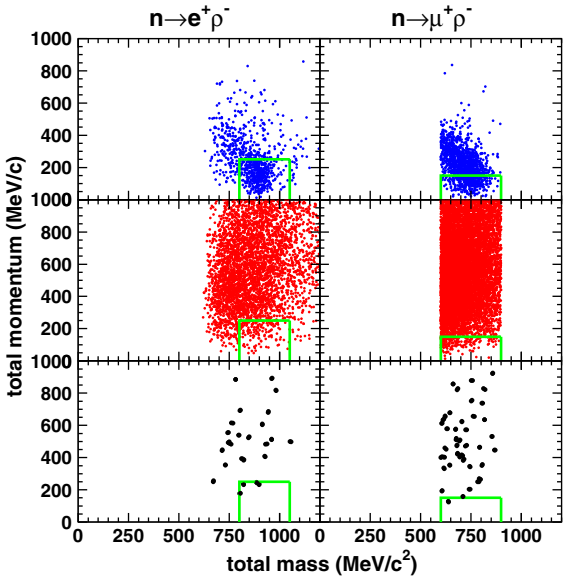

FIG. 20. Total invariant mass and total momentum for $n \to l^+\rho^-$ MC (top), atmospheric neutrino background MC corresponding to about 2000 years live time of SK (middle), and data (bottom) for $n \to e^+\rho^-$ (left) and $n \to \mu^+\rho^-$ (right) searches. All the event selections except (G6) in Sec. IV E are applied. The results from SK-I to SK-IV are combined. For the $n \to e^+\rho^-$ search, the signal box is shown as a green box. For the $n \to \mu^+\rho^-$ search, no total mass cut is applied in the analysis and the sharp cutoffs on the total mass correspond to the ρ^- mass cut threshold.

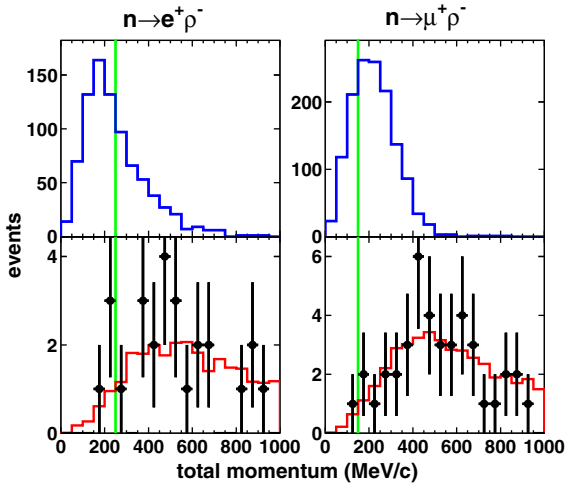

FIG. 21. Total momentum for $n \to l^+\rho^-$ MC (upper), atmospheric neutrino MC (lower, red histogram), and data (lower, black circles) for $n \to e^+\rho^-$ (left) and $n \to \mu^+\rho^-$ (right) searches. All the event selections except (G6) in Sec. IV E are applied. The atmospheric neutrino MC is normalized to data by area. Results from SK-I to SK-IV are combined. The signal region corresponds to the left side from the vertical green line. Total momenta of the data candidates are 173 MeV/c, 235 MeV/c, 239 MeV/c, 246 MeV/c for $n \to e^+\rho^-$ search and 129 MeV/c for $n \to \mu^+\rho^-$ search.

1.2% for the $n \to e^+\rho^-$ search. This is the lowest probability among all the nucleon decay searches and more details of these four events are described in Sec. V.

The one data candidate in SK-I in the $n \to e^+\rho^-$ search in this analysis was also selected in the previous analysis. There is one SK-II data candidate in both the $n \to e^+\rho^-$ and $n \to \mu^+\rho^-$ searches in this analysis. Both events were not selected in the previous analysis because their total momentum and mass were near the cut thresholds but outside of the signal box.

V. SEARCH RESULTS IN THE SK DATA

The signal selection efficiency, the number of the expected atmospheric neutrino backgrounds, and the number of data candidate events for each SK period are summarized in Table I.

For all the nucleon decay searches, the data and the atmospheric neutrino background MC agree with each other in both the event rates along the event selections and the relevant selection parameter distribution shapes shown in Sec. IV. There is no significant excess of data above the background expectation.

Thanks to the improvements of the 2008 electronics and data acquisition upgrade, the Michel electron tagging efficiency is higher and hence signal efficiency is improved in SK-IV, especially for nucleon decay modes including μ^+ in the final state. Likwise, the addition of neutron tagging has reduced the atmospheric neutrino background rate in SK-IV compared to SK-I-II-III while maintaining similar or higher signal efficiency.

The classification of background atmospheric neutrino interactions is shown in Table II. They are consistent with the previous analysis (Table V in [11]) within the statistical errors.

There are 12 data candidates in total (all the event displays in [26]). Back-to-back Cherenkov rings are visible and events are reconstructed as expected. All of the candidate events are near the total mass and momentum cut thresholds. For the SK-I and SK-II data samples, which have been reanalyzed for this paper, event migrations between the previous and current analysis can be explained by slight differences in the reconstructed parameters due to updates of the reconstruction algorithms as well as the detector calibrations.

The number of expected background events and data candidates as well as their Poisson probabilities are summarized in Table III. The number of detected events is consistent with the expected atmospheric neutrino background for all the searches.

The lowest probability (1.2%) is seen in the $n \to e^+\rho^-$ search. The number of events for each event selection step (Fig. 19) is in agreement with expectation leading up to the application of the momentum and mass signal region. In total, there are four data candidates. Their total invariant mass (MeV/c^2) and total momentum (MeV/c)

TABLE I. Summary of the signal efficiencies, the number of expected background events, and the number of data candidates for 91.5, 49.1, 31.8, and 143.8 kiloton · year exposure during SK-I, SK-II, SK-III, and SK-IV. For the $p \to l^+\eta$, $\eta \to 2\gamma$ searches, "upper" and "lower" stand for $100 < P_{\rm tot} < 250$ MeV/c and $P_{\rm tot} < 100$ MeV/c, respectively. Errors in the background events are statistical from finite MC statistics (about 500 years for each SK period). The number of expected background events scaled to 1 megaton · year are shown in parentheses.

	Efficiency (%)				Background (events)				Candidate (events)			
Modes	I	II	III	IV	I	II	III	IV	I	II	III	IV
$p \to e^+\eta$												
(2γ, upper)	11.0	10.9	10.7	9.8	$0.17 \pm 0.04 (1.8)$	$0.10 \pm 0.02 (2.0)$	$0.05 \pm 0.01 (1.5)$	$0.13 \pm 0.04 (0.92)$	0	0	0	0
(2γ, lower)	7.9	6.7	8.2	7.5	$0.01 \pm 0.01 (0.09)$	$0.01 \pm 0.01 (0.18)$	$0.003 \pm 0.003 (0.09)$	$0.01 \pm 0.01 (0.09)$	0	0	0	0
($3\pi^0$)	8.0	8.2	7.6	7.7	$0.15 \pm 0.03 (1.6)$	$0.06 \pm 0.02 (1.1)$	$0.06 \pm 0.01 (2.0)$	$0.03 \pm 0.02 (0.19)$	0	0	0	0
$p \to \mu^+\eta$												
(2γ, upper)	7.3	6.5	7.2	8.4	$0.05 \pm 0.02 (0.54)$	$0.02 \pm 0.01 (0.31)$	$0.01 \pm 0.01 (0.28)$	$0.03 \pm 0.01 (0.17)$	0	0	0	0
(2γ, lower)	5.8	5.6	6.0	7.0	$0 + 0.006 (0)$	$0 + 0.004 (0)$	$0 + 0.003 (0)$	$0 + 0.008 (0)$	0	0	0	0
($3\pi^0$)	6.9	6.2	6.9	7.9	$0.34 \pm 0.05 (3.7)$	$0.13 \pm 0.02 (2.7)$	$0.12 \pm 0.02 (3.7)$	$0.16 \pm 0.04 (1.1)$	0	1	0	1
$p \to e^+\rho^0$	3.8	3.3	3.6	3.8	$0.29 \pm 0.05 (3.2)$	$0.13 \pm 0.02 (2.6)$	$0.05 \pm 0.01 (1.4)$	$0.17 \pm 0.04 (1.2)$	0	0	0	2
$p \to \mu^+\rho^0$	1.9	1.3	2.2	1.9	$0.41 \pm 0.05 (4.4)$	$0.21 \pm 0.03 (4.4)$	$0.13 \pm 0.02 (4.0)$	$0.55 \pm 0.07 (3.8)$	1	0	0	0
$p \to e^+\omega$												
($\pi^0\gamma$)	2.3	2.5	2.3	2.1	$0.16 \pm 0.04 (1.7)$	$0.08 \pm 0.02 (1.6)$	$0.06 \pm 0.01 (1.8)$	$0.05 \pm 0.03 (0.36)$	0	0	0	0
($\pi^+\pi^-\pi^0$)	2.7	2.2	2.6	2.7	$0.44 \pm 0.06 (4.8)$	$0.17 \pm 0.03 (3.4)$	$0.12 \pm 0.02 (3.9)$	$0.27 \pm 0.06 (1.8)$	1	0	0	0
$p \to \mu^+\omega$												
($\pi^0\gamma$)	2.6	3.0	3.1	3.3	$0.18 \pm 0.04 (1.9)$	$0.10 \pm 0.02 (1.1)$	$0.08 \pm 0.01 (2.4)$	$0.07 \pm 0.03 (0.71)$	0	0	0	0
($\pi^+\pi^-\pi^0$)	3.1	2.6	3.2	4.6	$0.19 \pm 0.03 (2.0)$	$0.10 \pm 0.02 (1.1)$	$0.08 \pm 0.01 (2.5)$	$0.29 \pm 0.05 (2.0)$	0	0	0	0
$n \to e^+\pi^-$	12.7	12.2	13.5	12.6	$0.17 \pm 0.04 (1.9)$	$0.05 \pm 0.01 (1.1)$	$0.07 \pm 0.01 (2.0)$	$0.12 \pm 0.04 (0.83)$	0	0	0	0
$n \to \mu^+\pi^-$	11.3	10.7	11.5	13.4	$0.29 \pm 0.04 (3.1)$	$0.15 \pm 0.02 (3.0)$	$0.09 \pm 0.01 (2.9)$	$0.24 \pm 0.05 (1.7)$	0	0	1	0
$n \to e^+\rho^-$	1.4	1.1	1.4	1.5	$0.36 \pm 0.05 (3.9)$	$0.13 \pm 0.02 (2.7)$	$0.14 \pm 0.02 (4.4)$	$0.24 \pm 0.06 (1.6)$	1	1	2	0
$n \to \mu^+\rho^-$	1.0	1.0	1.1	1.2	$0.34 \pm 0.04 (3.7)$	$0.14 \pm 0.02 (2.8)$	$0.14 \pm 0.02 (4.3)$	$0.34 \pm 0.06 (2.4)$	0	1	0	0

are (884.7, 245.5), (821.5, 239.1), (897.7, 235.4), and (807.8, 173.2), respectively. Every candidate event is near the threshold of the selection window of the total mass and the momentum cut. The total invariant mass and momentum plots (Figs. 20 and 21) show that the data distributions agree with the expected atmospheric neutrino background distributions. Overall, we have concluded that the observed data candidates are due to atmospheric neutrino backgrounds.

The estimated signal efficiencies for $n \to l^+\pi^-$ with the charged pion in the final state are lower in this analysis than the previous analysis. For example, the signal efficiency for

TABLE II. The breakdown (percentage contribution) of the neutrino interaction modes of the background events [16]. The breakdowns are calculated by adding background events of the modes decaying into each meson from SK-I to SK-IV in total.

Mode	$p \to l^+\eta$	$p \to l^+\rho$	$p \to l^+\omega$	$n \to l^+\pi$	$n \to l^+\rho$
CCQE	4	9	1	22	4
CC 1-π	27	59	27	53	45
CC multi-π	21	10	32	11	13
CC others	23	1	8	3	3
NC	25	21	32	12	35

TABLE III. Summary of the nucleon decay searches. The number of events are summed from SK-I to SK-IV and for all the meson decay modes for each nucleon decay search. The events in the total signal box are shown for the $p \to l^+\eta$ search. The number of the expected atmospheric background events, along with systematic errors (see Table V for more details), is shown in the second column. The Poisson probability to observe events greater than or equal to the number of data candidates, without considering the systematic uncertainty in the background, is shown in the fourth column.

Modes	Background (events)	Candidate (events)	Probability (%)	Lifetime Limit ($\times 10^{33}$ years) at 90% CL
$p \to e^+\eta$	0.78 ± 0.30	0	···	10.
$p \to \mu^+\eta$	0.85 ± 0.23	2	20.9	4.7
$p \to e^+\rho^0$	0.64 ± 0.17	2	13.5	0.72
$p \to \mu^+\rho^0$	1.30 ± 0.33	1	72.7	0.57
$p \to e^+\omega$	1.35 ± 0.43	1	74.1	1.6
$p \to \mu^+\omega$	1.09 ± 0.52	0	···	2.8
$n \to e^+\pi^-$	0.41 ± 0.13	0	···	5.3
$n \to \mu^+\pi^-$	0.77 ± 0.20	1	53.7	3.5
$n \to e^+\rho^-$	0.87 ± 0.26	4	1.2	0.03
$n \to \mu^+\rho^-$	0.96 ± 0.28	1	61.7	0.06
total	8.6	12	15.7	···

the $n \to e^+\pi^-$ search in SK-I decreased from 19.4% to 12.7%. This is due to the improved pion interaction model which better matches external data. As shown in Fig. 2, the cross sections for all the interactions are increased around 500 MeV/c. The larger cross sections reduce the number of the visible Cherenkov rings, with reduction of the estimated signal efficiency mainly coming from the corresponding event selection.

A. Systematic errors

The total systematic errors in the signal efficiency and the number of expected background events are summarized in Tables IV and V. The systematic error sources consist of uncertainties of physics models in the nucleon decay MC, the atmospheric neutrino background MC, and event reconstruction performance. The systematic error estimation methods are the same as in the previous analysis, with several improvements that allow us to significantly reduce the errors.

Table IV shows the systematic errors in the signal efficiencies for each systematic error source. The dominant systematic errors come from uncertainties of the meson interactions in the oxygen nucleus (meson nuclear effect). The meson nuclear effect errors are smaller in the lower signal box for $p \to l^+\eta$ and $\eta \to 2\gamma$ searches thanks to the large fraction of the free proton decays.

In this analysis, the systematic uncertainties of pion interactions are evaluated by varying the tuning parameters of the interaction models within 1σ uncertainties of $\pi^{\pm}$-nucleus experimental data. This method provides a more reliable evaluation of systematic uncertainties of the pion interactions compared to the previous paper [11], especially for higher-momentum ($\geq$500 MeV/c) pions. This method leads to relatively smaller systematic uncertainties of the pion interactions in signal and atmospheric neutrino background events than the previous analysis.

In the previous analysis [11] the uncertainty in Fermi momentum distribution was estimated by artificially rescaling the distribution by 20%. While being simple, this is a rather crude procedure. In this work, we improve and provide a more precise uncertainty estimate by directly comparing the momentum distributions, simulated using a spectral function fit to the ^{12}C electron scattering data [15], to the simulated atmospheric background momentum distribution from NEUT, which uses a relativistic Fermi gas model. The difference between the two is taken as a systematic error.

Uncertainties associated with event reconstruction are implemented as detector performance errors. The error sources include: vertex position, number of Cherenkov rings, particle identification (e/μ separation), the number of Michel electrons, and the energy scale. In the previous study, the error estimate was overly conservative and included an additional contribution from the effects of artificially shifting the vertex by 30 cm. We do not adopt such a contribution in this work.

Table V shows the systematic errors in the number of expected background events for each systematic error source. After the event selection, the raw number of the remaining expected background events is either zero or one in the lower signal box for $p \to l^+\eta$, $\eta \to 2\gamma$ searches. Therefore, the systematic errors are estimated in the total box ($P_{\rm tot} < 250$ MeV/c) and assumed to be the same both

TABLE IV. Summary of systematic errors (percentage contribution) on signal efficiencies for each error source. The errors from SK-I to SK-IV are averaged by the live time. For $p \to l^+\eta$, $\eta \to 2\gamma$ searches, "upper" and "lower" stand for $100 < P_{\rm tot} < 250$ MeV/c and $P_{\rm tot} < 100$ MeV/c, respectively.

Modes	Meson nuclear effect	Hadron propagation in water	N-N correlated decay	Fermi momentum	Detector performances	Total
$p \to e^+\eta$ (2γ, upper)	26	···	8	9	2	29
$p \to e^+\eta$ (2γ, lower)	9	···	3	13	2	16
$p \to e^+\eta$ ($3\pi^0$)	12	···	4	15	4	20
$p \to \mu^+\eta$ (2γ, upper)	27	···	9	10	3	30
$p \to \mu^+\eta$ (2γ, lower)	11	···	3	12	3	17
$p \to \mu^+\eta$ ($3\pi^0$)	17	···	6	2	5	19
$p \to e^+\rho^0$	9	13	1	4	6	17
$p \to \mu^+\rho^0$	10	9	1	2	10	17
$p \to e^+\omega$ ($\pi^0\gamma$)	14	···	3	14	4	20
$p \to e^+\omega$ ($\pi^+\pi^-\pi^0$)	14	6	3	0.4	7	17
$p \to \mu^+\omega$ ($\pi^0\gamma$)	14	···	1	2	3	14
$p \to \mu^+\omega$ ($\pi^+\pi^-\pi^0$)	24	5	2	1	4	25
$n \to e^+\pi^-$	13	7	11	1	4	19
$n \to \mu^+\pi^-$	15	7	10	3	4	20
$n \to e^+\rho^-$	60	3	9	5	5	61
$n \to \mu^+\rho^-$	48	5	3	12	8	50

TABLE V. Summary of systematic errors (percentage contribution) on the number of expected background events for each error source. The errors from SK-I to SK-IV are averaged by the live time. For $p \to l^+\eta$, $\eta \to 2\gamma$ searches, "upper" and "lower" stand for $100 < P_{\rm tot} < 250$ MeV/c and $P_{\rm tot} < 100$ MeV/c, respectively.

Modes	Neutrino flux	Neutrino cross section	Pion nuclear effect	Hadron propagation in water	Detector performances	Total
$p \to e^+\eta$ (2γ, upper)	8	15	12	5	21	30
$p \to e^+\eta$ (2γ, lower)	8	15	12	5	21	30
$p \to e^+\eta$ ($3\pi^0$)	8	12	34	17	30	51
$p \to \mu^+\eta$ (2γ, upper)	9	15	14	8	28	37
$p \to \mu^+\eta$ (2γ, lower)	9	15	14	8	28	37
$p \to \mu^+\eta$ ($3\pi^0$)	8	12	9	13	12	25
$p \to e^+\rho^0$	4	18	10	7	15	27
$p \to \mu^+\rho^0$	7	16	5	11	14	25
$p \to e^+\omega$ ($\pi^0\gamma$)	8	15	21	5	32	42
$p \to e^+\omega$ ($\pi^+\pi^-\pi^0$)	6	15	7	14	17	28
$p \to \mu^+\omega$ ($\pi^0\gamma$)	8	13	18	8	28	37
$p \to \mu^+\omega$ ($\pi^+\pi^-\pi^0$)	8	10	22	46	16	55
$n \to e^+\pi^-$	7	17	6	10	24	32
$n \to \mu^+\pi^-$	8	16	3	6	17	26
$n \to e^+\rho^-$	7	16	15	16	11	30
$n \to \mu^+\rho^-$	5	20	15	4	14	29

in the upper and lower boxes. With the improved error estimation method, the systematic errors in the most dominant systematic error source in the previous analysis, hadron propagation in water, are reduced by a factor of three to five in this analysis.

B. Lifetime limit

All of the observed events are consistent with the expected backgrounds and nucleon lifetime limits are calculated as in [7,11] using the Bayes method to incorporate systematic uncertainty. The limits are calculated by combining different search methods as well as different SK periods for each nucleon decay search. All of the nucleon decay searches except $p \to l^+\eta$ have four measurements corresponding to four SK periods. As in the previous analysis, the signal efficiencies and the backgrounds are added for $p \to l^+\omega$ mode with two different meson decay modes $\omega \to \pi^0\gamma$ and $\omega \to \pi^+\pi^-\pi^0$. There are 12 measurements for $p \to l^+\eta$ searches corresponding to three methods per each of the four SK periods, where the three methods come from upper and lower signal boxes for $\eta \to 2\gamma$ search and one signal box for $\eta \to 3\pi^0$ search.

The conditional probability distribution for each nucleon decay rate is expressed as

$$P(\Gamma|n_i) = \iiint \frac{e^{-(\Gamma\lambda_i\epsilon_i+b_i)}(\Gamma\lambda_i\epsilon_i+b_i)^{n_i}}{n_i!} \times P(\Gamma)P(\lambda_i)P(\epsilon_i)P(b_i)d\lambda_i d\epsilon_i db_i, \quad (4)$$

where n_i is the number of data candidate events in the ith measurement, λ_i is the true detector exposure, ϵ_i is the true selection efficiency, and b_i is the true number of background events. The decay rate prior probability distribution $P(\Gamma)$ is 1 for $\Gamma \geq 0$ and otherwise 0. $P(\lambda_i)$, $P(\epsilon_i)$, and $P(b_i)$ are the prior probability distributions for detector exposure, efficiency, and background, respectively, which are assumed to be Gaussian distributions. The uncertainty on the exposure is assumed to be 1% for all SK periods.

The upper limit of the nucleon decay rate, $\Gamma_{\rm limit}$, is

$$\mathrm{CL} = \frac{\int_{\Gamma=0}^{\Gamma_{\rm limit}} \prod_{i=1}^{N} P(\Gamma|n_i)d\Gamma}{\int_{\Gamma=0}^{\infty} \prod_{i=1}^{N} P(\Gamma|n_i)d\Gamma}, \quad (5)$$

where N is the number of measurements for each nucleon decay search and CL is the confidence level taken to be 90%. The partial lower lifetime limit for each nucleon decay mode is given by

$$\tau/\mathrm{B} = \frac{1}{\Gamma_{\rm limit}}. \quad (6)$$

The nucleon partial lifetime limits at 90% confidence level are summarized in Table III. The limits range from 3×10^{31} to 1×10^{34} years. Thanks to the addition of SK-III and SK-IV data and various analysis improvements, the lifetime limits published in this paper are typically higher than those in the previous analysis by a factor of two to three, as shown in Fig. 22. However, some channels show similar or even lower limits due to more observed data candidates.

Figure 22 compares the updated SK results with the other experiments: IMB-3 [27], KAMIOKANDE-I+II [28], and FREJUS [29]. The updated SK results are better than those

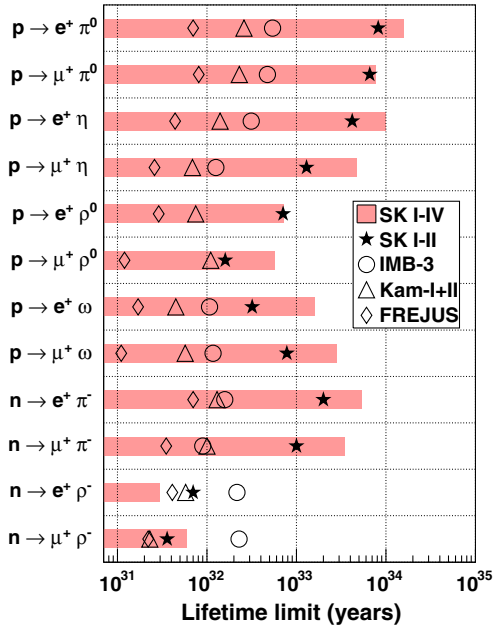

FIG. 22. Explored ranges and lower limits of nucleon partial lifetime with the results of the other experiments [27–29] and the previous SK analysis [11]. The $p \to l^+\pi^0$ results [7] are also included.

by the other experiments by one to two orders of magnitude except for the $n \to l^+\rho^0$ channel. The relatively lower performance is due to low signal efficiencies with tight event selections and nonzero data candidates in the SK analyses. Note that systematic errors in the signal efficiencies were not included in the IMB-3 limit, and thus the published results were optimistic.

VI. CONCLUSION

The survey of nucleon decay into charged antilepton plus meson by Super-Kamiokande based on only SK-I and SK-II data [11] has been updated to include improved event reconstruction algorithms, event selections, systematic error estimations, and an additional 0.175 megaton · years of SK-III and SK-IV data. A similar update for the $p \to l^+\pi^0$ search by Super-Kamiokande has also been published recently [7].

Using 0.316 megaton · years of data, no significant excess is found above the expected atmospheric neutrino background. The number and features of candidate events are consistent with the background estimation by the atmospheric neutrino MC. Therefore, partial lifetime limits are set ranging from 3×10^{31} to 1×10^{34} years at 90% confidence level depending on the nucleon decay mode. The lifetime limits are summarized in Table III.

Most of the results presented here are world-best limits, and they further constrain the relevant GUT models.

ACKNOWLEDGMENTS

We gratefully acknowledge the cooperation of the Kamioka Mining and Smelting Company. The Super-Kamiokande experiment has been built and operated from funding by the Japanese Ministry of Education, Culture, Sports, Science and Technology, the U.S. Department of Energy, and the U.S. National Science Foundation. Some of us have been supported by funds from the National Research Foundation of Korea NRF-2009-0083526 (KNRC) funded by the Ministry of Science, ICT, and Future Planning, the European Union H2020 RISE-GA641540-SKPLUS, the Japan Society for the Promotion of Science, the National Natural Science Foundation of China under Grants No. 11235006, the National Science and Engineering Research Council (NSERC) of Canada, the Scinet and Westgrid consortia of Compute Canada, and the National Science Centre of Poland (2015/17/N/ST2/04064, 2015/18/E/ST2/00758).

[1] H. Georgi and S. L. Glashow, Unity of All Elementary Particle Forces, Phys. Rev. Lett. **32**, 438 (1974).
[2] H. Fritzsch and P. Minkowski, Unified interactions of leptons and hadrons, Ann. Phys. (N.Y.) **93**, 193 (1975).
[3] P. Nath and P. Fileviez Perez, Proton stability in grand unified theories, in strings and in branes, Phys. Rep. **441**, 191 (2007).
[4] G. Senjanovic, Proton decay and grand unification, AIP Conf. Proc. **1200**, 131 (2010).
[5] P. Langacker, Grand unified theories and proton decay, Phys. Rep. **72**, 185 (1981).
[6] M. Machacek, The decay modes of the proton, Nucl. Phys. **B159**, 37 (1979); M. B. Gavela, A. Le Yaouanc, L. Oliver, O. Pene, and J. C. Raynal, Exclusive modes of proton decay in SU(5), Phys. Lett. **98B**, 51 (1981); J. F. Donoghue, Proton lifetime and brancing rations in SU(5), Phys. Lett. **92B**, 99 (1980); F. Buccella, G. Miele, L. Rosa, P. Santorelli, and T. Tuzi, An upper limit for the proton lifetime in SO(10), Phys. Lett. B **233**, 178 (1989).
[7] K. Abe *et al.* (Super-Kamiokande Collaboration), Search for proton decay via $p \to e + \pi^0$ and $p \to \mu + \pi^0$ in 0.31 megaton·years exposure of the Super-Kamiokande water Cherenkov detector, Phys. Rev. D **95**, 012004 (2017).
[8] Y. Fukuda *et al.* (Super-Kamiokande Collaboration), The Super-Kamiokande detector, Nucl. Instrum. Methods Phys. Res., Sect. A **501**, 418 (2003); K. Abe *et al.* (Super-Kamiokande Collaboration), Calibration of the Super-Kamiokande detector, Nucl. Instrum. Methods Phys. Res., Sect. A **737**, 253 (2014).

[9] H. Nishino, K. Awai, Y. Hayato, S. Nakayama, K. Okumura, M. Shiozawa, A. Takeda, K. Ishikawa, A. Minegishi, and Y. Arai, High-speed charge-to-time converter ASIC for the Super-Kamiokande detector, Nucl. Instrum. Methods Phys. Res., Sect. A **610**, 710 (2009); S. Yamada *et al.* (Super-Kamiokande Collaboration), Commissioning of the new electronics and online system for the Super-Kamiokande experiment, IEEE Trans. Nucl. Sci. **57**, 428 (2010).

[10] M. Shiozawa, Reconstruction algorithms in the Super-Kamiokande large water Cherenkov detector, Nucl. Instrum. Methods Phys. Res., Sect. A **433**, 240 (1999).

[11] H. Nishino *et al.* (Super-Kamiokande Collaboration), Search for nucleon decay into charged antilepton plus meson in Super-Kamiokande I and II, Phys. Rev. D **85**, 112001 (2012).

[12] H. Ejiri, Nuclear deexcitations of nucleon holes associated with nucleon decays in nuclei, Phys. Rev. C **48**, 1442 (1993).

[13] T. J. Irvine, Ph.D. Thesis, University of Tokyo, 2014.

[14] T. Yamazaki and Y. Akaishi, Nuclear medium effects on invariant mass spectra of hadrons decaying in nuclei, Phys. Lett. B **453**, 1 (1999).

[15] K. Nakamura, S. Hiramatsu, T. Kamae, H. Muramatsu, N. Izutsu, and Y. Watase, The reaction C-12 (e, e' p) at 700-MeV and DWIA analysis, Nucl. Phys. **A268**, 381 (1976).

[16] Y. Hayato, NEUT, Nucl. Phys. B, Proc. Suppl. **112**, 171 (2002); G. Mitsuka, NEUT, AIP Conf. Proc. **967**, 208 (2007); NEUT, AIP Conf. Proc. **981**, 262 (2008).

[17] L. L. Salcedo, E. Oset, M. J. Vicente-Vacas, and C. Garcia-Recio, Computer Simulation of Inclusive Pion Nuclear Reactions, Nucl. Phys. **A484**, 557 (1988).

[18] R. A. Giannelli *et al.*, Multiproton final states in positive pion absorption below the Delta (1232) resonance, Phys. Rev. C **61**, 054615 (2000); A. Saunders, S. Hoibraten, J. J. Kraushaar, B. J. Kriss, R. J. Peterson, R. A. Ristinen, J. T. Brack, G. Hofman, E. F. Gibson, and C. L. Morris, Reaction and total cross sections for low-energy pi+ and pi- on isospin zero nuclei, Phys. Rev. C **53**, 1745 (1996); I. Navon, D. Ashery, J. Alster, G. Azuelos, B. M. Barnett, W. Gyles, R. R. Johnson, D. R. Gill, and T. G. Masterson, True absorption and scattering of 50-MeV pions, Phys. Rev. C **28**, 2548 (1983); T. J. Bowles *et al.*, Inclusive ($\pi^{\pm}$, π^0) reactions in nuclei, Phys. Rev. C **23**, 439 (1981); D. Ashery, I. Navon, G. Azuelos, H. K. Walter, H. J. Pfeiffer, and F. W. Schleputz, True absorption and scattering of pions on nuclei, Phys. Rev. C **23**, 2173 (1981); D. Ashery *et al.*, Inclusive pion single charge exchange reactions, Phys. Rev. C **30**, 946 (1984); S. M. Levenson *et al.*, Inclusive pion scattering in the Delta (1232) region (1232), Phys. Rev. C **28**, 326 (1983); M. K. Jones *et al.*, Pion absorption above the Delta (1232) resonance, Phys. Rev. C **48**, 2800 (1993); P. Chavanon, M. Crozon, T. Leray, and J. Tocqueville, Determination of the pion neutral angular distribution in the reaction π^+, $p \to \pi^+$, p, π^0 in the energy range 600 to 1300 MeV (in french), Phys. Lett. **28B**, 296 (1968); T. Takahashi *et al.*, π^-—^{12}C elastic scattering above the Δ resonance, Phys. Rev. C **51**, 2542 (1995); B. W. Allardyce *et al.*, Pion reaction cross sections and nuclear sizes, Nucl. Phys. **A209**, 1 (1973); J. W. Cronin, R. Cool, and A. Abashian, Cross sections of nuclei for high-energy pions, Phys. Rev. **107**, 1121 (1957); K. Aoki *et al.*, Elastic and inelastic scattering of pi+ and pi- on C12 at 995 MeV/c, Phys. Rev. C **76**, 024610 (2007); A. Rahav *et al.*, Measurement of the C-12(pi,2pi) Reactions and Possible Evidence of a Double Delta Excitation, Phys. Rev. Lett. **66**, 1279 (1991).

[19] G. I. Lykasov, W. Cassing, A. Sibirtsev, and M. V. Rzyanin, ωN final state interactions and ω-meson production from heavy-ion collisions , Eur. Phys. J. A **6**, 71 (1999).

[20] M. Honda, T. Kajita, K. Kasahara, and S. Midorikawa, Improvement of low energy atmospheric neutrino flux calculation using the JAM nuclear interaction model, Phys. Rev. D **83**, 123001 (2011).

[21] H. W. Bertini, Intranuclear-cascade calculation of the secondary nucleon spectra from nucleon-nucleus interactions in the energy range 340 to 2900 MeV and comparisons with experiment, Phys. Rev. **188**, 1711 (1969).

[22] J. O. Johnson and T. A. Gabriel, Report No. ORNL/TM-10340, 1988.

[23] S. Mine *et al.* (K2K Collaboration), Experimental study of the atmospheric neutrino backgrounds for $p \to e^+\pi^0$ searches in water Cherenkov detectors, Phys. Rev. D **77**, 032003 (2008).

[24] Y. Ashie *et al.*, Measurement of atmospheric neutrino oscillation parameters by Super-Kamiokande I, Phys. Rev. D **71**, 112005 (2005).

[25] C. Regis *et al.*, Search for proton decay via $p \to \mu + K^0$ in Super-Kamiokande I, II, and III, Phys. Rev. D **86**, 012006 (2012).

[26] See Supplemental Material at http://link.aps.org/supplemental/10.1103/PhysRevD.96.012003 for graphical event displays of the candidate events.

[27] C. McGrew *et al.* (IMB Collaboration), Search for nucleon decay using the IMB-3 detector, Phys. Rev. D **59**, 052004 (1999).

[28] K. S. Hirata *et al.* (Kamiokande Collaboration), Experimental limits on nucleon lifetime for lepton + meson decay modes, Phys. Lett. B **220**, 308 (1989).

[29] C. Berger *et al.* (Frejus Collaboration), Results from the Frejus experiment on nucleon decay modes with charged leptons, Z. Phys. C **50**, 385 (1991).